Front. Earth Sci. 2015, 9(4): 691–699
DOI 10.1007/s11707-015-0529-0

RESEARCH ARTICLE

Multiple-scale temporal variations and fluxes near a hydrothermal vent over the Southwest Indian Ridge

Xiaodan CHEN[1], Chujin LIANG (✉)[1], Changming DONG[2,3], Beifeng ZHOU[1], Guanghong LIAO[1], Junde LI[1]

1 State Key Lab of Satellite Ocean Environment Dynamics, Second Institute of Oceanography, Hangzhou 310012, China
2 School of Marine Sciences, Nanjing University of Information Science and Technology, Nanjing 210044, China
3 Department of Atmospheric and Oceanic Sciences, University of California, Los Angeles, CA 90001, USA

© Higher Education Press and Springer-Verlag Berlin Heidelberg 2015

Abstract A deep-ocean mooring system was deployed 100 m away from an active hydrothermal vent over the Southwest Indian Ridge (SWIR), where the water depth is about 2,800 m. One year of data on ocean temperature 50 m away from the ocean floor and on velocities at four levels (44 m, 40 m, 36 m, and 32 m away from the ocean floor) were collected by the mooring system. Multiple-scale variations were extracted from these data: seasonal, tidal, super-tidal, and eddy scales. The semidiurnal tide was the strongest tidal signal among all the tidal constituents in both currents and temperature. With the multiple-scale variation presented in the data, a new method was developed to decompose the data into five parts in terms of temporal scales: time-mean, seasonal, tidal, super-tidal, and eddy. It was shown that both eddy and tidal heat (momentum) fluxes were characterized by variation in the bottom topography: the tidal fluxes of heat and momentum in the along-isobath direction were much stronger than those in the cross-isobath direction. For the heat flux, eddy heat flux was stronger than tidal heat flux in the cross-isobath direction, while eddy heat flux was weaker in the along-isobath direction. For the momentum flux, the eddy momentum flux was weaker than tidal momentum flux in both directions. The eddy momentum fluxes at the four levels had a good relationship with the magnitude of mean currents: it increased with the mean current in an exponential relationship.

Keywords multiple-scale analysis, tidal flux, eddy flux

1 Introduction

The Southwest Indian Ridge (SWIR) is an ultraslow spreading ridge with a length of 7,700 km, separating the African and Antarctic plates (Tao et al., 2011; Zhang and Tao, 2011). Recently, the SWIR has received extensive attention in terms of marine geologic study (Muller et al., 2000; Minshull et al., 2006; Li et al., 2008). Cao and Cao (2011) conducted studies on tectonic settings, hydrothermal activities and geochemical features in the SWIR. Zhang and Gao (2011) focused on the geological and geophysical characters of the interaction between hotspot and ridge. One of the most interesting discoveries along the SWIR is that an active hydrothermal vent was found during a Chinese research cruise DY 115-19 in 2007, which is located at 37°47′S, 49°39′E (Tao et al., 2012). It is the first active hydrothermal field found along the ultraslow spreading ridge (Tao et al., 2011). The ridge segment where the hydrothermal vent is located parallels the zonal direction (Huang et al., 2009). The surface current near the hydrothermal vent is the westward drift, and the abyssal water is the circumpolar deep water (CDW) (Leblond, 1976; Emery and Meincke, 1986), which is a mixture of the North Atlantic Deep Water (NADW), Antarctic Bottom Water (AABW), Antarctic Intermediate Water (AAIW), and recirculated deep water from the Indian and Pacific (Santoso et al., 2006). The CDW has temperature from 0.1°C to 2.0°C and salinity from 34.62 to 34.73 ppt (Emery and Meincke, 1986). The Mozambique and Crozet basins are open to the Antarctic, so the bottom water can enter directly from the south, and the deep northward flow close to Madagascar is conjectured to flow from the Crozet Basin through θ-S characteristics or other properties (Warren, 1974; Kolla et al., 1976a, b; Warren, 1978). Though the abyssal flow is northwestward from the Antarctic Ocean (Reid, 2003), the local direction is subject to change forced by the geostrophic constraint (see Section 3).

Understanding the hydrodynamic processes around a hydrothermal vent is important for the investigation of

Received December 27, 2014; accepted April 6, 2015

E-mail: cjliang@sio.org.cn

physical processes around the hydrothermal plume and related mechanisms. Hydrodynamic processes can help explain the spatial distribution of light scattering, temperature and manganese or other chemical elements' concentrations along the rift valley (Edmonds et al., 2003). It can also help the development of numerical modeling studies for hydrothermal plumes (e.g., Morton et al., 1956; Middleton and Thomson, 1986; Speer and Rona, 1989; Crone and Wilcock, 2005; Wichers, 2005). Such *in-situ* measurements in the deep ocean are rare, due to the high cost. In this paper, we analyze the hydrographic data obtained from a deep-ocean mooring deployed near the above-mentioned hydrothermal vent over the SWIR to study multiple-scale heat and momentum fluxes.

The rest of the paper is organized as follows. Section 2 describes the observational data and analysis method. Section 3 is the results from the analysis. Discussion and summary are presented in Section 4.

2 Observational data and methodology

2.1 Observational data

A mooring system was deployed at (49.649°E, 37.7830°S), at about 2,800 m in depth. The site is about 100 m west of the hydrothermal vent (49.650°E, 37.7833°S). These two locations are too close to be seen in Fig. 1, so they are marked by one red star. The topography clearly shows that the isobath is almost parallel to the zonal direction. Therefore, we call the zonal direction the along-isobath direction, and the meridional direction as the cross-isobath direction in this paper.

The structure of the mooring system is presented in Fig. 2. This is a bottom-moored system: a downward-looking 300-kHz Acoustic Doppler Current Profiler (ADCP) fixed on a cable at 50 m above the sea floor. Data at four levels are validated: 44 m, 40 m, 36 m, and 32 m above the sea floor; and the data were sampled every 15 minutes. The currents are projected onto the along-isobath and cross-isobath directions. In addition, a thermal meter is available at 50 m above the sea floor. The mooring system was deployed from January 15, 2009 to January 1, 2010, collecting nearly one full year data.

2.2 Methodology

Oceanic data can be decomposed into two parts: time-mean and deviation from the mean. The latter is considered as an eddy-contributed variation. In the deep ocean where the wind forcing cannot reach, tidal forcing is the dominant external forcing. Near a hydrothermal vent where heat is occasionally released, extra variation could be from the heat release. Therefore, hydrodynamic processes near a vent could show multiple scales. In this study, we develop the following new method to decompose all measured variables into multiple scales and study their fluxes in the deep ocean.

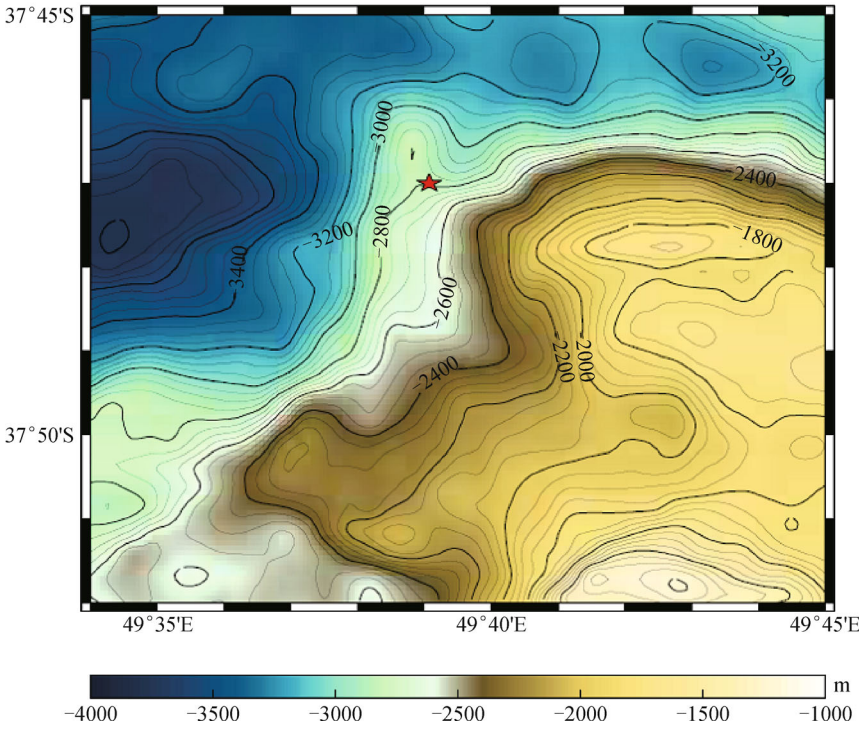

Fig. 1 Location of the hydrothermal vent (red star). The active hydrothermal field is located at (37°47′S, 49°39′E) along the SWIR. The mooring system is about 100 m away from the hydrothermal vent, which is not distinctive from the vent in the figure.

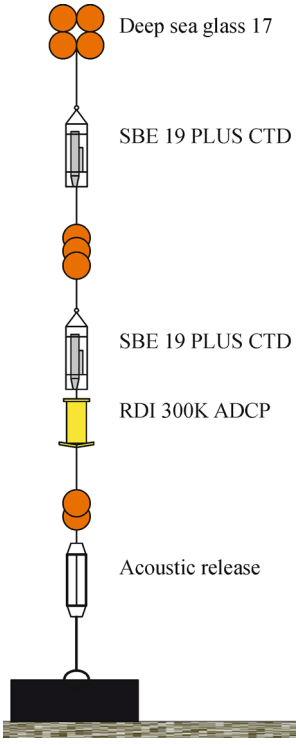

Fig. 2 The structure of the mooring system: a downward-looking 300-kHz ADCP, with a temperature sensor (not shown), is fixed at 50 m above the ocean bottom.

Instead of decomposing a variable into time mean and deviation with respect to the mean, we decompose the horizontal components (u and v) of velocity and temperature (T) into five parts: the time average ($\overline{u}$, $\overline{V}$, $\overline{T}$), seasonal signal (u_s, v_s, T_s), tidal component (u_t, v_t, T_t), high-frequency signal (u_h, v_h, T_h), and perturbation component (u_e, v_e, T_e):

$$u = \overline{u} + u_s + u_t + u_h + u_e, \tag{1}$$

$$v = \overline{v} + v_s + v_t + v_h + v_e, \tag{2}$$

$$T = \overline{T} + T_s + T_t + T_h + T_e. \tag{3}$$

Let $u_p = u - \overline{u} - u_s - u_h$, $v_p = v - \overline{v} - v_s - v_h$, $T_p = T - \overline{T} - T_s - T_h$, u_p, v_p, T_p can be considered as perturbations with respect to the long-term mean after the high-frequency oscillation and seasonal signals are removed. Conventionally, the cross products of the deviational parts of temperature are called eddy heat flux (H_x, H_y), and the cross products of the deviational parts of velocities, as eddy momentum fluxes (M_{xx}, M_{yy}, M_{xy}). Based on Eqs. (1)–(3), the deviational parts of the variables include two parts: regular tidal parts and eddy-induced variation,

$$u_p = u_t + u_e, \tag{4}$$

$$v_p = v_t + v_e, \tag{5}$$

$$T_p = T_t + T_e. \tag{6}$$

Then, one can obtain

$$\begin{aligned} H_x = \overline{u_p T_p} &= \overline{(u_t + u_e)(T_t + T_e)} \\ &= \overline{u_t T_t} + \overline{u_t T_e} + \overline{u_e T_t} + \overline{u_e T_e}. \end{aligned} \tag{7}$$

Following the similar process, one can have

$$H_y = \overline{v_p T_p} = \overline{v_t T_t} + \overline{v_t T_e} + \overline{v_e T_t} + \overline{v_e T_e}, \tag{8}$$

$$M_{xx} = \overline{u_p u_p} = \overline{u_t u_t} + \overline{u_t u_e} + \overline{u_e u_t} + \overline{u_e u_e}, \tag{9}$$

$$M_{yy} = \overline{v_p v_p} = \overline{v_t v_t} + \overline{v_t v_e} + \overline{v_e v_t} + \overline{v_e v_e}, \tag{10}$$

$$M_{xy} = \overline{u_p v_p} = \overline{u_t v_t} + \overline{u_t v_e} + \overline{u_e v_t} + \overline{u_e v_e}. \tag{11}$$

In this study, we use T-TIDE harmonic analysis package (Pawlowicz et al., 2002) to extract the tidal signals of u_t, v_t, T_t. The time mean is the one averaged over the entire length of the data, i.e., yearly-mean.

From Eqs. (7)–(11), we can see the fluxes have four terms: tidal flux (the first term), tidal-eddy interaction flux (the second and third terms) and eddy flux (the fourth term). In Section 3, we will show that the tidal-eddy interaction flux is one order smaller than tidal flux or eddy flux, and can be neglected.

3 Results

3.1 Multiple-scale variability

Though the observation was far away from the sea surface (about 2,800 m from the surface), both the currents and temperature showed multiple-scale variability: seasonal, intra-seasonal (eddy), tidal (diurnal and semi-diurnal), and super-tidal (frequency higher than the tides) scales. The super-tidal frequency is not of interest to the presented study.

3.1.1 Seasonal variability

At the mooring site, the current persistently flowed westward with a daily-averaged speed of 0.36–11.10 cm/s, which can clearly be seen from the time series of vertical averages of the current data at four levels in Fig. 3. The average direction of the velocity was about 278 degrees (clockwise from north, and the north is 0 degrees), almost aligned with the isobath (Fig. 1), which implies the mean current was controlled by the bottom topography. The daily-averaged sea water temperature (T) at 50 m in Fig. 3 shows the varying range of the daily-averaged

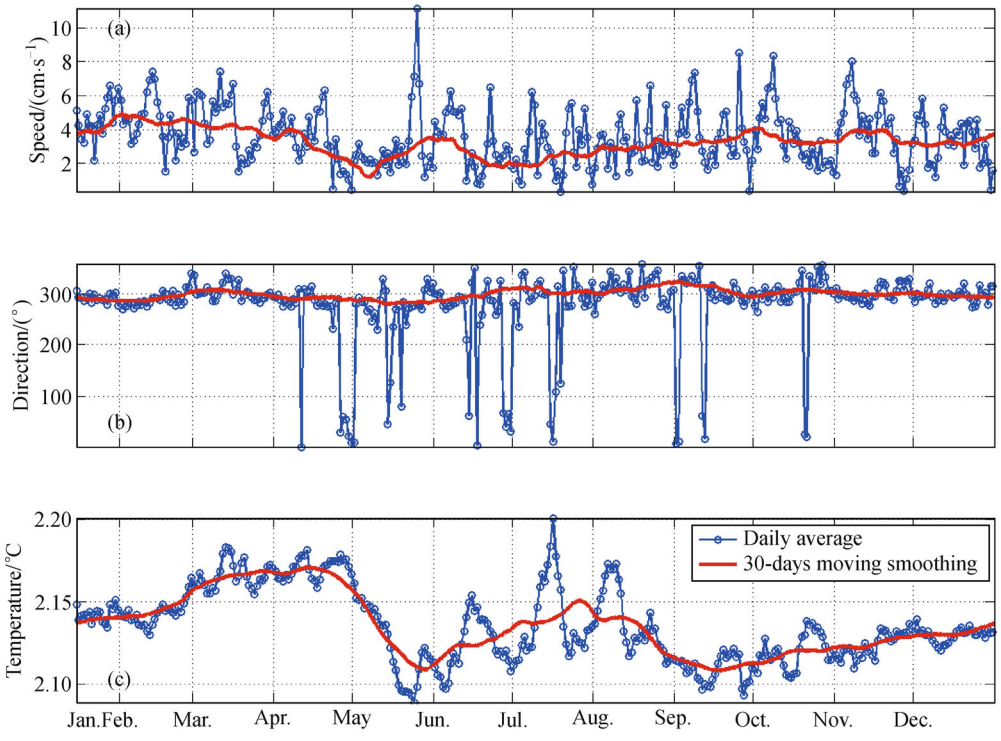

Fig. 3 Daily-averaged time series of current speed (a), direction (b), and temperature (c) (at 50 m above the ocean floor). Blue and red curves denote daily-averaged and 30-day-moving-smoothed values, respectively.

temperature of 2.08°C−2.20°C.

With 30-day-moving average applied to smooth the data, the seasonal variations in both velocity and temperature are presented through a period of about three months. Such seasonal variation might be a reflection of the seasonal variation in the large-scale circulation, which is still unclear.

3.1.2 Intra-seasonal (Eddy-scale) variability

The intra-seasonal variation is evident in the velocity and temperature time series, shown in Fig. 3, which is associated with eddy activities or the heat release from the nearby hydrothermal vent. The peaks in the temperature time series could be associated with the activity of the hydrothermal vent, as the mooring system was located almost west of the vent, and the westward flow might transport warm water from the vent to the mooring site. Their time scales are in the order of 10 days.

3.1.3 Tidal variability

A spectral analysis is applied to the vertically-averaged velocity and measured temperature. We find that the spectral density of the temperature (Fig. 4) had the dominant frequency of 0.08 cycles per hour (cph), corresponding to the semidiurnal M2 and S2 tidal constituents, and two smaller spikes occurred at about 0.16 and 0.25 cph, which correspond to M4 and M6, respectively. The along-isobath velocity (U) and cross-isobath velocity (V) were similar to the temperature, with the above-mentioned three spikes at these specific frequencies; but they also had a spike at the diurnal tidal period (K1 and O1) with a frequency of 0.04 cph.

We calculate 13 tidal constituents. The two leading tidal constituents are M2 and S2, and their tidal ellipses (eastward is 0 degrees, turning anticlockwise) are shown in Fig. 5. The inclination of M2 is roughly 163 degrees, and S2 is 0.3−10.0 degrees, decreasing from 44 m to 32 m. M2 was northwestward, consistent with the daily-averaged current, with a direction of 300 degrees (northward is 0 degrees, turning clockwise in Fig. 3). The major axis of M2 was about 5 cm/s. M2 was dominant at this site where the hydrothermal vent is located nearby. The semidiurnal tidal period was the dominant period in the area.

In summary, the velocity and temperature in the deep ocean near the hydrothermal vent experienced multiple-scale variations: tidal variation, intra-seasonal variation and seasonal variation. The tidal variation was dominated by the semi-diurnal tides, intra-seasonal variation was from eddy variation or the activity of the nearby hydrothermal

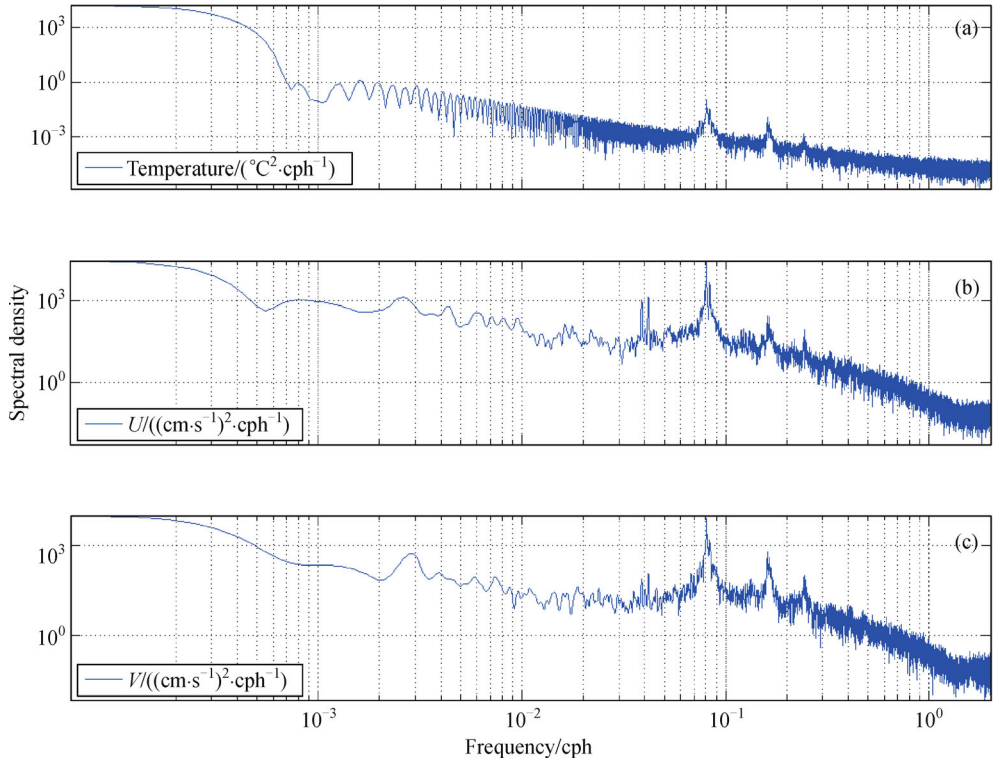

Fig. 4 Spectral density of (a) seawater temperature and (b, c) vertically-averaged currents ((b) along-isobath velocity *U*; (c) cross-isobath velocity *V*). Obviously, semidiurnal tidal signals dominate in both currents and temperature.

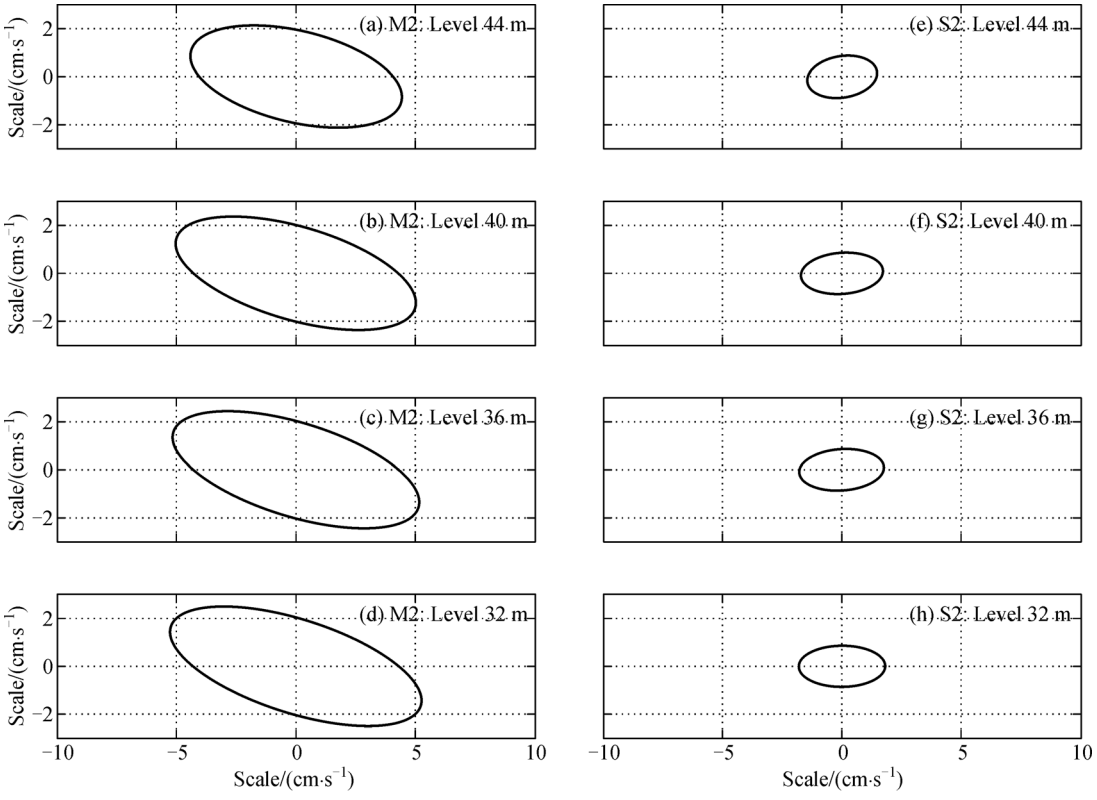

Fig. 5 Tidal ellipses of the two leading tidal constituents: (a) M2: at 44 m; (b) M2: at 40 m; (c) M2: at 36 m; (d) M2: at 32 m; (e) S2: at 44 m; (f) S2: at 40 m; (g) S2: at 36 m; (h) S2: at 32 m. Tidal vectors turn clockwise.

vent, and seasonal variation might be from a large-scale background circulation.

3.2 Tidal and eddy fluxes

Following Eq. (7)−(11), we calculate the four terms in the deviational flux. The heat flux is calculated at 50 m above the sea floor, where only temperature measurements are available. Since the velocity data are not available at 50 m, we use the velocity measurement at the nearest depth (44 m). The momentum flux is calculated at the four depths.

Using Eqs. (7)−(11), we compute yearly average of the four terms on the right hand side of each equation. Note that two cross terms are zero theoretically as they are the products of variables with different frequencies. Figures 6 and 7 demonstrate that the cross products of tidal and eddy signals can be neglected compared with the other two terms of tidal flux and eddy flux.

From Fig. 6, the eddy fluxes of $\overline{U_eT_e}$ and $\overline{V_eT_e}$ are 0.005 and 0.0019 cm/(s·°C), respectively, while the tidal fluxes of $\overline{U_tT_t}$ and $\overline{V_tT_t}$ are about 0.020 and 0.0013 cm/(s·°C), respectively. The tidal (eddy) flux in the along-isobath direction was much larger than that in the cross-isobath direction. In the along-isobath direction, the tidal heat flux was four times of the eddy flux, while in the cross-isobath direction the tidal flux was only two-third of the eddy flux. Therefore, in the cross-isobath direction the heat flux was dominated by the eddy heat flux, while in the along-isobath direction the heat flux was controlled by the tidal heat flux. It can be explained that the tidal current amplitude in the along-isobath direction was much stronger than that in the cross-isobath direction (see Fig. 5).

Figure 7 shows that the tidal momentum flux of $\overline{U_tU_t}$ ranges from 12.8 to 18.2 cm^2/s^2, $\overline{V_tV_t}$ is about 2.7 to 3.7 cm^2/s^2, and $\overline{U_tV_t}$ is −4.3 to −1.9 cm^2/s^2. Again, the cross-isobath flux of $\overline{V_tV_t}$ was much smaller than the along-isobath flux of $\overline{U_tU_t}$.

Also shown in Fig. 7, the eddy momentum flux of $\overline{U_eU_e}$ is from 3.0 to 4.2 cm^2/s^2, while $\overline{V_eV_e}$ is 1.00 to 1.35 cm^2/s^2, $\overline{U_eV_e}$ is −0.31 to −0.05 cm^2/s^2. The eddy momentum flux was weaker than the tidal momentum flux. Compared with the tidal momentum flux, in the along-isobath direction, the eddy momentum flux was about 25% of the tidal momentum flux. In the cross-isobath direction, the eddy momentum flux was one third of the tidal momentum flux. At the four levels, such ratios between the tidal and eddy fluxes remained similar.

It should be noted that the eddy heat flux in the cross-isobath direction was stronger than the tidal heat flux, but the eddy momentum flux in the cross-isobath direction was weaker than the tidal momentum flux. The difference could be caused by the heat release from the nearby hydrothermal vent.

3.3 Relationship between eddy flux and mean current

Figure 8 shows that the eddy momentum flux had a good relationship with the mean velocity $\overline{U}$ ($\overline{V}$). The eddy flux

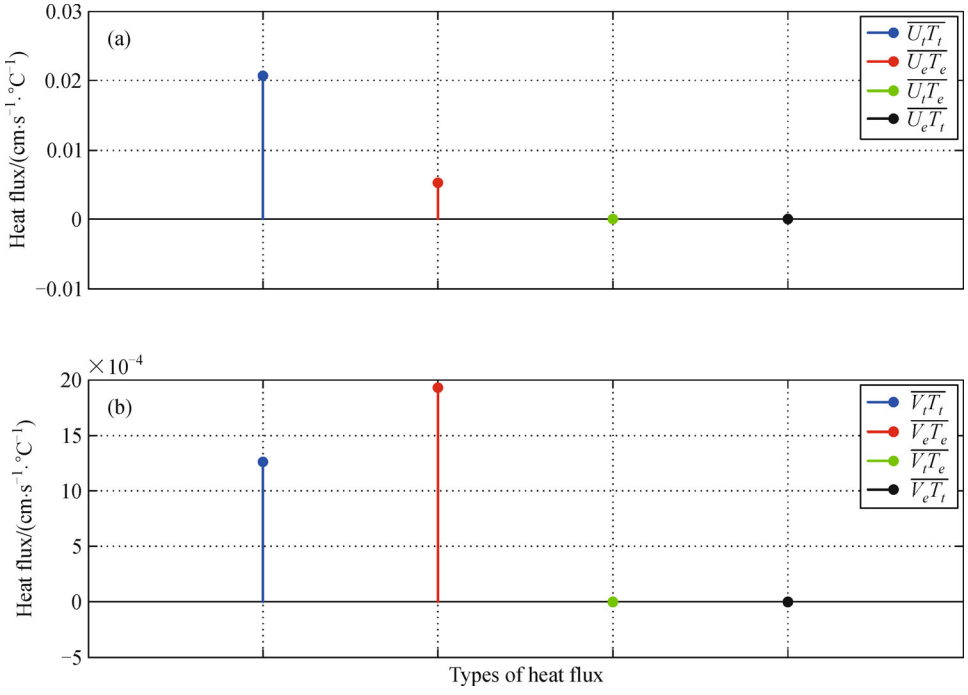

Fig. 6 Heat fluxes at 50 m away from the sea floor: (a) along-isobath direction and (b) cross-isobath direction. Blue indicates tidal heat flux, red represents eddy heat flux and the remaining colors denote cross terms.

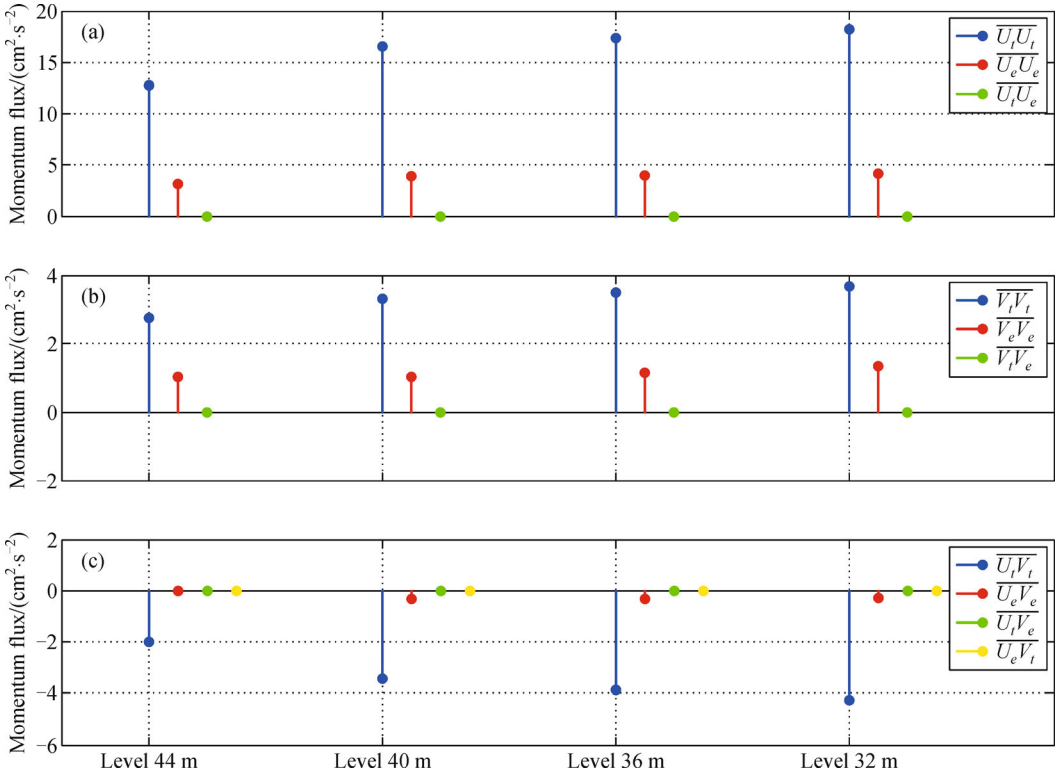

Fig. 7 Momentum fluxes at four levels: (a) along-isobath, (b) cross-isobath and (c) along-cross-isobath. Blue indicates tidal momentum flux, red represents eddy momentum flux and the remaining colors denote cross terms.

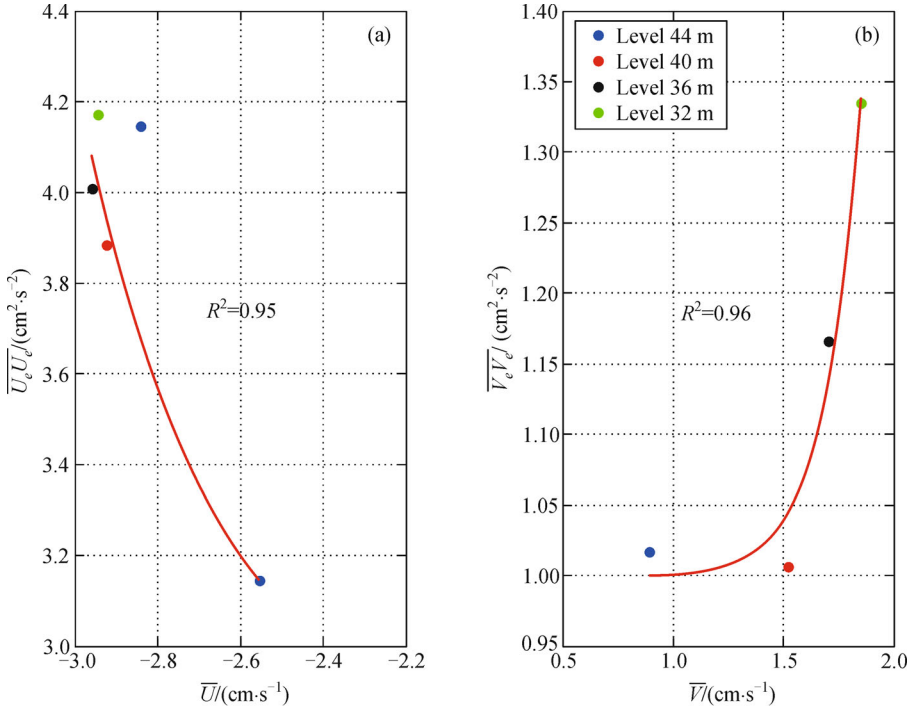

Fig. 8 Yearly-averaged eddy flux vs. mean current velocity. (a) Eddy momentum flux in the along-isobath direction. (b) Eddy momentum flux in the cross-isobath direction. The red line is a regression line.

increased with the magnitude of the mean velocity, and the relationship can be regressed into an exponential function:

$$\overline{U_e U_e} = 2.793 + 9.72*10^{-5}*\exp\left(-3.2097*\overline{U}\right), \quad (12)$$

$$\overline{V_e V_e} = 0.9984 + 4.85*10^{-6}*\exp\left(6.0238*\overline{V}\right). \quad (13)$$

Such relationship could be useful in the estimate of bottom stress in a numerical study (Rooth, 1972; Faria et al., 1998; Feddersen et al., 2000; Dong et al., 2009).

4 Summary

Based on the limited measurement data from a mooring system near a hydrothermal vent over the SWIR, we conducted multiple-scale analysis on the hydrographic data. It was found that both the currents and temperature had multiple-scale variations at the seasonal, intra-seasonal, tidal, and super-tidal scales. The current persistently flowed westward with a daily-averaged speed within 0.36−11.10 cm/s at the mooring site. Semidiurnal tides were dominant at the site for both currents and temperature.

Based on the multiple-scale variations present in the temperature and velocity data, a new decomposition method was introduced to analyze the tidal and eddy fluxes: both temperature and velocity were decomposed into five parts: time-mean, seasonal, tidal, super-tidal, and eddy. The tidal and eddy fluxes were analyzed in detail, which demonstrated that heat and momentum fluxes in the deep ocean were different between the along- and cross-isobath directions. The variation in topography played an important role in the deep ocean. Both the tidal heat and momentum fluxes in the along-isobath direction were much stronger than those in the cross-isobath direction. In the cross-isobath direction, the eddy heat flux was stronger than the tidal heat flux while the tidal momentum flux was stronger than eddy flux. It could be caused by the occasional heat release from the hydrothermal vent. The eddy momentum fluxes at the four levels had a good relationship with the mean currents: the eddy momentum flux increased with the magnitude of the mean velocity, in an exponential relationship.

Since the observational system only carried one thermal meter, we cannot conduct the eddy heat flux similar to the analysis on the momentum flux. Also due to the limitation of the observational data (only one station), we cannot conduct the horizontal gradient of the horizontal eddy flux. However, the present observational data and analysis illustrated the interesting multiple-scale processes in the deep ocean.

Acknowledgements The data used in this paper are from Chinese DY115-21 cruise. We thank all the staff for their hard work, especially our colleague Tao Ding, who brought back the mooring system successfully and acquired these invaluable observational data. We express our sincere gratitude to Weifang Jin and Tao Ding, for their help during the early-stage data processing. This study was support by the National Basic Research Program of China on hydrothermal plume characteristics and environmental effects (No. 2012CB417303), the project of global change and interaction between ocean and atmosphere (GASI-03-01-01-07). CD appreciates the support from the National Natural Science Foundation of China (Grant Nos. 41376033, 41476022, and 41490640), and the NUIST startup grants. We appreciate Jian Zhu's help to make Figure 1.

References

Cao H, Cao Z (2011). Review of submarine hydrothermal activities in Southwest Indian Ridge. Marine Geology and Quaternary Geology, 31(1): 67–75 (in Chinese)

Crone T J, Wilcock W S (2005). Modeling the effects of tidal loading on mid-ocean ridge hydrothermal systems. Geochem Geophys Geosyst, 6(7): n/a doi: 10.1029/2004GC000905

Dong C, Idica E Y, McWilliams J C (2009). Circulation and multiple-scale variability in the Southern California Bight. Prog Oceanogr, 82 (3): 168–190

Edmonds H N, Michael P J, Baker E T, Connelly D P, Snow J E, Langmuir C H, Dick J B, Mühe R, German C R, Graham D W (2003). Discovery of abundant hydrothermal venting on the ultraslow-spreading Gakkel ridge in the Arctic Ocean. Nature, 421 (6920): 252–256

Emery W J, Meincke J (1986). Global water masses-summary and review. Oceanol Acta, 9(4): 383–391

Faria A F, Thornton E B, Stanton T P, Soares C V, Lippmann T C (1998). Vertical profiles of longshore currents and related bed shear stress and bottom roughness. Journal of Geophysical Research: Oceans (1978–2012), 103(C2): 3217–3232

Feddersen F, Guza R T, Elgar S, Herbers T H C (2000). Velocity moments in alongshore bottom stress parameterizations. Journal of Geophysical Research: Oceans (1978–2012), 105(C4): 8673–8686

Huang W, Tao C, Deng X, Zhou J, Sun Y, Dou B, Liu W (2009). Discussion and the scientific significance of IODP drilling to study in the 49°39′E vent field in Southwest Indian Ridge. Journal of Marine Sciences, 27(02): 97–103 (in Chinese)

Kolla V, Henderson L, Biscaye P E (1976a). Clay mineralogy and sedimentation in the western Indian Ocean. Deep-Sea Res, 23(10): 949–961

Kolla V, Sullivan L, Streeter S S, Langseth M G (1976b). Spreading of Antarctic bottom water and its effects on the floor of the Indian Ocean inferred from bottom-water potential temperature, turbidity, and sea-floor photography. Mar Geol, 21(3): 171–189

LeBlond P H (1976). Temperature-salinity analysis of world ocean waters. Journal of the Fisheries Board of Canada, 33(6): 1471

Li X, Chu F, Lei J, Zhao J (2008). Advances in slow-ultraslow-spreading Southwest Indian Ridge. Advances in Earth Science, 23(6): 595–603 (in Chinese)

Middleton J M, Thomson R E (1986). Modelling the rise of hydrothermal plumes. Canadian Technical Report of Hydrography and Ocean Science, 69: 1–18

Minshull T A, Muller M R, White R S (2006). Crustal structure of the Southwest Indian Ridge at 66 E: seismic constraints. Geophys J Int,

166(1): 135–147

Morton B R, Taylor G, Turner J S (1956). Turbulent gravitational convection from maintained and instantaneous sources. Proc R Soc Lond A Math Phys Sci, 234(1196): 1–23

Muller M R, Minshull T A, White R S (2000). Crustal structure of the Southwest Indian Ridge at the Atlantis II fracture zone. Journal of Geophysical Research: Solid Earth (1978–2012), 105(B11): 25809–25828

Pawlowicz R, Beardsley B, Lentz S (2002). Classical tidal harmonic analysis including error estimates in MATLAB using T_TIDE. Comput Geosci, 28(8): 929–937

Reid J L (2003). On the total geostrophic circulation of the Indian Ocean: flow patterns, tracers, and transports. Prog Oceanogr, 56(1): 137–186

Rooth C (1972). A linearized bottom friction law for large-scale oceanic motions. J Phys Oceanogr, 2(4): 509–510

Santoso A, England M H, Hirst A C (2006). Circumpolar deep water circulation and variability in a coupled climate model. J Phys Oceanogr, 36(8): 1523–1552

Speer K G, Rona P A (1989). A model of an Atlantic and Pacific hydrothermal plume. Journal of Geophysical Research: Oceans (1978–2012), 94(C5): 6213–6220

Tao C, Li H, Huang W, Han X, Wu G, Su X, Zhou N, Lin J, He Y H, Zhou J P (2011). Mineralogical and geochemical features of sulfide chimneys from the 49°39′E hydrothermal field on the Southwest Indian Ridge and their geological inferences. Chin Sci Bull, 56(26): 2828–2838

Tao C, Lin J, Guo S, Chen Y, Wu G, Han X, German C R, Yoerger D R, Zhou N, Li H, Su X, Zhu J (2012). First active hydrothermal vents on an ultraslow-spreading center: Southwest Indian Ridge. Geology, 40 (1): 47–50

Warren B A (1974). Deep flow in the Madagascar and Mascarene basins. Deep-Sea Res, 21(1): 1–21

Warren B A (1978). Bottom water transport through the Southwest Indian Ridge. Deep-Sea Res, 25(3): 315–321

Wichers S (2005). Verification of numerical models for hydrothermal plume water through field measurements at TAG. Dissertation for PhD Degree. Massachusetts Institute of Technology

Zhang T, Gao J (2011). Characters of magmatic activity and tectonics on the ultraslow spreading ridge in Southwest Indian ocean. Advances in Marine Science, 29(03): 314–322 (in Chinese)